Poling of an artificial magneto-toroidal crystal

Author(s):
Lehmann, Jannis; Donnelly, Claire; Derlet, Peter M.; Heyderman, Laura J.; Fiebig, Manfred

Publication date:
2019-02

Permanent link:
https://doi.org/https://doi.org/10.3929/ethz-b-000310648

Originally published in:
Nature Nanotechnology 14(2), https://doi.org/10.1038/s41565-018-0321-x

Funding acknowledgement:
- "Resonant optical magnetoelectric effect in magnetic nanostructures" ()

nature nanotechnology

LETTERS

https://doi.org/10.1038/s41565-018-0321-x

Poling of an artificial magneto-toroidal crystal

Jannis Lehmann[1*], Claire Donnelly[2,3], Peter M. Derlet[4], Laura J. Heyderman[2,3] and Manfred Fiebig[1*]

Although ferromagnetism is known to be of enormous importance, the exploitation of materials with a compensated (for example, antiferromagnetic) arrangement of long-range ordered magnetic moments is still in its infancy. Antiferromagnetism is more robust against external perturbations, exhibits ultrafast responses of the spin system[1] and is key to phenomena such as exchange bias[2,3], magnetically induced ferroelectricity[4] or certain magnetoresistance phenomena[5]. However, there is no conjugate field for the manipulation of antiferromagnetic order, hindering both its observation and direct manipulation. Only recently, direct poling of a particular antiferromagnet was achieved with spintronic approaches[6]. An interesting alternative to antiferromagnetism is ferrotoroidicity—a recently established fourth form of ferroic order[7,8]. This is defined as a vortex-like magnetic state with zero net magnetization, yet with a spontaneously occurring toroidal moment[9]. As a hallmark of ferroic order, there must be a conjugate field that can manipulate the order parameter. For ferrotoroidic materials, this is a toroidal field—a magnetic vortex field violating both space-inversion and time-reversal symmetry analogous to the toroidal moment[10]. However, the nature and generation of the toroidal field remain elusive for conventional crystalline systems. Here, we demonstrate the creation of an artificial crystal[11,12] consisting of mesoscopic planar nanomagnets with a magneto-toroidal-ordered ground state. Effective toroidal fields of either sign are applied by scanning a magnetic tip over the crystal. Thus, we achieve local control over the orientation of the toroidal moment despite its zero net magnetization.

The ferrotoroidic order parameter is the so-called toroidization, derived from the toroidal moment $\mathbf{t} = \sum_i \mathbf{r}_i \times \mathbf{m}_i$, where $\mathbf{r}_i$ and $\mathbf{m}_i$ are the position and magnetic moment of the ith atom within the unit cell, see Fig. 1c. In a crystal, individual toroidal moments $\mathbf{t}_j$ of the jth unit cell align uniformly to yield a ferrotoroidic state with a spontaneous macroscopic toroidization, $\mathbf{T} = \sum_j \mathbf{t}_j$ (refs [7,10]). Both experiments[13,14] and theory[15] have confirmed that ferrotoroidicity constitutes a fourth form of primary ferroic order in addition to ferromagnetism, ferroelectricity and ferroelasticity[8]. So far, toroidal poling has been achieved by reproducing the symmetry conditions of the toroidal field, with the simultaneous application of perpendicular magnetic and electric fields[14]. This drives a magnetoelectric interaction, but the coupling to the actual toroidal field remains unclear.

Here we transfer the concept of magnetization-free ferrotoroidic order and toroidal field poling to the mesoscopic scale by designing arrays of ferromagnetic nanoelements, whose moments form a ferrotoroidic ground state. Two-dimensional periodic arrays of submicrometre-sized single-domain nanomagnets, which represent giant Ising spins, have proven to be a valuable testing ground for magnetic correlations[11,12,16]. A well-studied example is artificial spin ice—a frustrated system in which emergent magnetic monopoles[17], phase transitions[18,19] and long-range order[20–22] have been observed. Externally applied magnetic fields, as well as thermal annealing, have been employed to modify the magnetic configuration of these patterns[17,22–25].

Two-dimensional dipolar-coupled arrays of elongated permalloy ($Ni_{81}Fe_{19}$) nanomagnets are shown in Fig. 1a. The magnetic force microscopy (MFM) image in Fig. 1b reveals that a toroidal state with domains of either toroidization, $\pm\mathbf{T}$, forms spontaneously

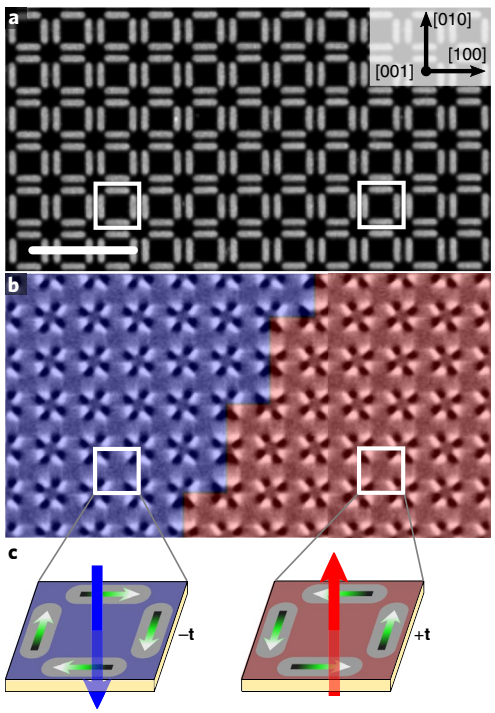

Fig. 1 | Artificial magneto-toroidal crystal. a, Atomic force microscopy image of an artificial magneto-toroidal crystal built from 450 × 150 × 20 nm³ permalloy nanomagnets (fabricated on a silicon substrate) with 11 × 6 unit cells (as shown in **c**) and with a lattice constant of 830 nm (the whole array contains 68 × 68 unit cells). Unit cells comprising four nanomagnets are highlighted by the white boxes. Scale bar: 2 µm. **b**, Corresponding magnetic force microscopy image revealing an as-grown toroidal domain structure with a domain boundary separating states of opposite toroidization. **c**, The orientation of the toroidal moment, +**t** (red arrow) or −**t** (blue arrow), depends on the handedness of the arrangement of the magnetic moments (green arrows) in the unit cell.

[1]Laboratory for Multifunctional Ferroic Materials, Department of Materials, ETH Zurich, Zurich, Switzerland. [2]Laboratory for Mesoscopic Systems, Department of Materials, ETH Zurich, Zurich, Switzerland. [3]Laboratory for Multiscale Materials Experiments, Paul Scherrer Institute, Villigen, Switzerland. [4]Condensed Matter Theory Group, Paul Scherrer Institute, Villigen, Switzerland. *e-mail: jannis.lehmann@mat.ethz.ch; manfred.fiebig@mat.ethz.ch

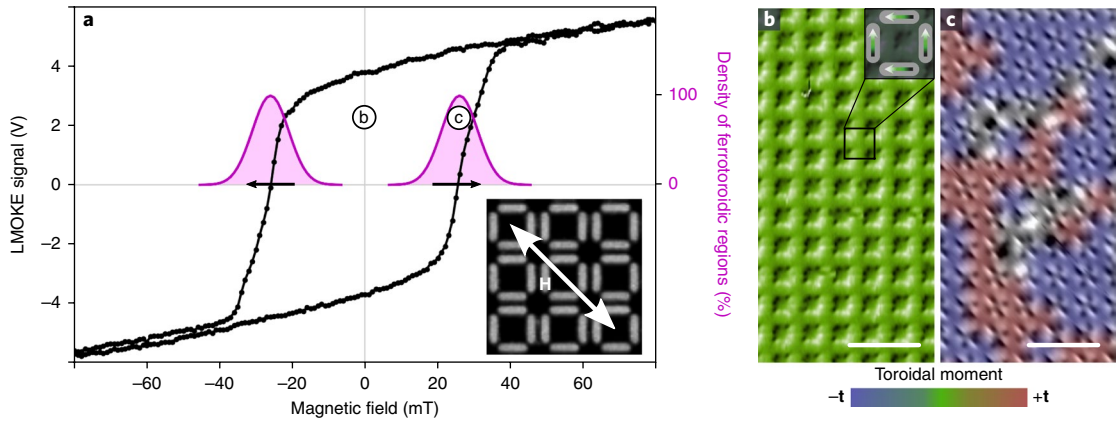

Fig. 2 | Magnetization curve and ferrotoroidic ground state. a, In-plane magnetization of the two-dimensional array of nanomagnets from Fig. 1 measured with the longitudinal magneto-optical Kerr effect (LMOKE) as a function of a magnetic field **H** applied along the [110] direction. Purple curves are Gaussian fits of $|\partial \mathbf{M}/\partial \mathbf{H}|$ (with **M** as the measured magnetization component and **H** as the applied magnetic field), and indicate the areal density of ferrotoroidic regions, which peaks around the coercive magnetic field. **b**, MFM image of the ferromagnetic single-domain state at remanence. Inset, a corresponding unit cell. **c**, MFM image of the multi-domain ferrotoroidic state at the coercive magnetic field. The colour bar represents the value of the toroidal moment, with a range from −**t** to +**t**. Scale bars: 2 μm.

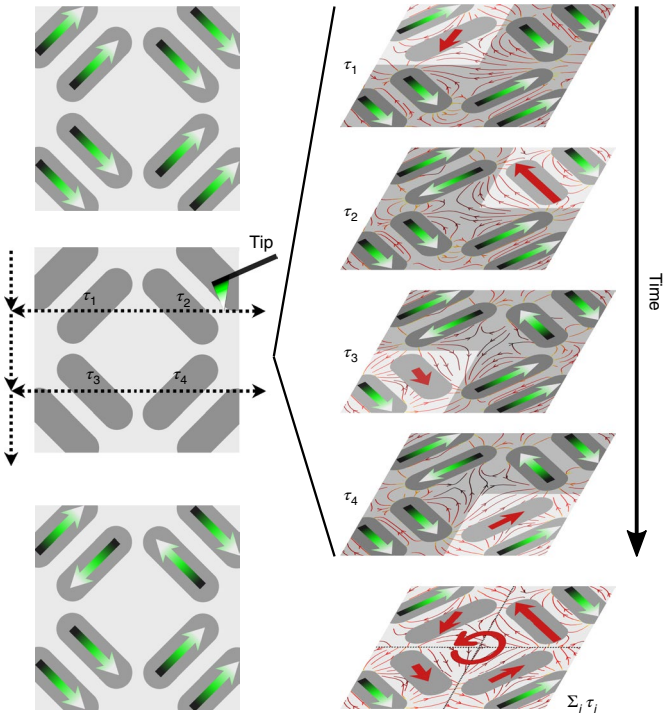

Fig. 3 | Generation of a toroidal poling field at the mesoscale. Left, schematic of the top-to-bottom magnetic-tip scanning process for a mesoscopic unit cell within our artificial magneto-toroidal crystal. Shown are the initial state with net magnetization along the [110] direction (top), a sketch of the scanning process with the tip trajectory indicated by dashed arrows (middle) and the final magneto-toroidal state with toroidization along the [001] direction (bottom). Right, sequential tip-assisted destabilization and reorientation of the nanomagnets. The magnetic field exerted by the magnetic moments (green arrows) is indicated by red contours. The bold red arrow represents the net value of the local magnetic field at the position of the respective nanomagnet above which the tip hovers in time steps τ_1 to τ_4. The direction of this net magnetic field (see Methods) determines whether the nanomagnet will reverse its magnetization (τ_1 and τ_2) or remain unswitched (τ_3 and τ_4). The combination of the four time steps (bottom right) yields an effective toroidal field (red circular arrow) at the level of the unit cell.

in the as-grown sample. In transferring the magnetic order from the atomic to the mesoscale, we have replaced exchange interactions with magnetic–dipolar interactions as the basis of this ferroic order[26,27]. The presence of long-range order with distinct domain states, which is uniquely associated with the orientation of an order parameter (see Fig. 1c), distinguishes the ordered state in the magneto-toroidal crystal fundamentally from the long-range order observed in artificial spin ice[20–22]. It should also be noted that magnetic elements with intrinsic vortex states have been explored as potential memory cells or for high-density data storage[28,29]. In arrays of such magnetic elements, each element can carry a local toroidal moment. However, because of the intentionally weak coupling between the elements, crosstalk is negligible by design so that long-range order and domains, which are key to the functionality of the magneto-toroidal crystal, are not present.

Preference for the ferrotoroidic state in our magneto-toroidal crystal is confirmed with a cycled in-plane magnetic field. Measurements of the longitudinal magneto-optical Kerr effect (LMOKE; see Methods) probe the in-plane net magnetization **M** of the array. We observe a hysteresis loop, shown in Fig. 2a, in which a magnetic field of ±40 mT drives the array into a uniformly magnetized state that is spatially resolved in Fig. 2b. At the coercive field of ±27 mT, the net magnetization is compensated. Remarkably, instead of forming a state with an equal distribution of +**M** and −**M** domains as in a ferromagnet, our system exhibits a ferrotoroidic ±**T** multi-domain pattern, as shown in Fig. 2c. The spontaneous occurrence of toroidal domains confirms the ferrotoroidic nature of our system, bestowing a physical identity on the concept of ferrotoroidicity. In contrast to previous work on weakly coupled magnetic vortex elements[28], there is no built-in geometric asymmetry to enforce a uniform vorticity in the entire sample. Rather, our toroidal order occurs spontaneously as a consequence of the long-range dipolar coupling between the nanomagnets. The spontaneous nature of the toroidal order provides the freedom to choose between two different degenerate domain states, and thus allows the formation of a multi-domain pattern.

The domain pattern seen in Fig. 2c also demonstrates that a global magnetic field cannot induce a single-domain +**T** or −**T** ferrotoroidic state. This would require the application of a toroidal field **S** as the conjugate field of ferrotoroidic order. The application of **S** introduces an imbalance in the free energy, $F \propto \mathbf{S} \cdot \mathbf{T}$, between opposite toroidal domain states, and therefore promotes a single

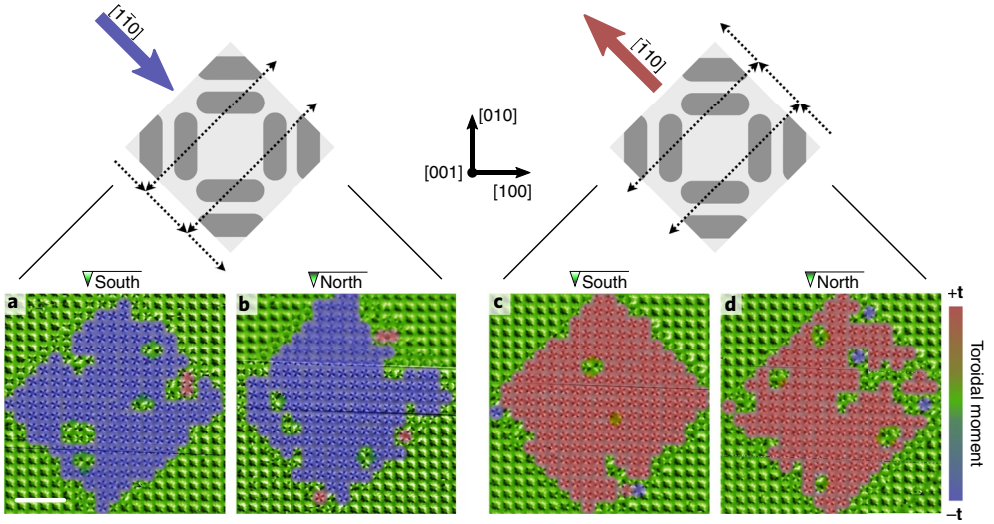

Fig. 4 | Experimental demonstration of magneto-toroidal poling. a–d, MFM images of four regions of an artificial magneto-toroidal crystal to which toroidal poling fields +S or −S were applied as calculated (see Methods and Fig. 3). Scale bar: 4 μm. The different combinations of slow-scan directions (blue and red block arrows), the tip trajectory (dashed arrows) and out-of-plane tip magnetizations ('North','South') are shown schematically above the images. Note that the sign of the toroidal poling field (−S in **a** and **b**; and +S in **c** and **d**; see Fig. 3 and Methods) determines the resulting orientation of the toroidal moment (see colour bar) and depends on the slow-scan direction but not on the magnetization direction of the tip.

domain. This is analogous to the formation of uniform magnetization $\mathbf{M}$ in a ferromagnet in response to a magnetic field $\mathbf{H}$ via $F \propto \mathbf{H} \cdot \mathbf{M}$. Until now, the local application of a toroidal field has not been achieved. Here, we demonstrate its application to a mesoscopic toroidal crystal.

Our toroidal poling (see Fig. 3) is based on the MFM-tip-assisted reorientation of individual nanomagnets. As a first step, a global magnetic field is used to uniformly align all magnets into a remanent state with $\mathbf{M}||[110]$. The magnetic tip is then scanned line-by-line at 10 μm s^{-1} along the ±[110] 'fast' direction, while the net motion of the tip is in the [1$\bar{1}$0] 'slow' direction. Whenever the tip passes across a nanomagnet, the local energy landscape is modified by the MFM-tip field[23,25] such that the magnetization of the nanomagnet is destabilized. As a result, the nanomagnet becomes susceptible to reorientation due to the local field exerted by the surrounding magnets. Using a model system of anisotropic point-dipoles arranged in a lattice (data not shown), we have confirmed that there is a 'perturbation' regime where the tip field only catalyses the process and does not contribute to the poling of the nanomagnets. In Fig. 3, the four essential time steps τ_1 to τ_4 of this procedure are depicted for a representative unit cell defined by the central four magnets. The net field acting on the tip-destabilized nanomagnet, which originates from the surrounding magnets, is derived from a micromagnetic finite-element calculation (see Methods) and is represented by a red arrow. This net field determines the new direction of the magnetization of the nanomagnet. The combination of steps τ_1 to τ_4 shown at the bottom right of Fig. 3 reveals that, most strikingly, our MFM-tip scan results in an effective toroidal field. Since the unit cell shown in Fig. 3 represents the entire crystal lattice, we thus obtain a time-integrated global toroidal field that is applied to the entire area scanned by the MFM tip.

We verified the toroidal poling procedure experimentally by scanning an MFM tip across areas of the crystal as shown in Fig. 4. Apart from a few local defects, the four areas are homogeneously poled in either the $+\mathbf{T}$ or $-\mathbf{T}$ orientations, using an effective conjugate toroidal field ($\pm\mathbf{S}_{\mathrm{eff}}$). The reversal of the slow-scan direction (between Fig. 4a,b and Fig. 4c,d) introduces time reversal into the poling process such that $\mathbf{S}_{\mathrm{eff}}$, and thus $\mathbf{T}$, reverses its sign. The reversal of the initial magnetization of the sample is equivalent to a rotation of the sample by 180°, and therefore is equivalent to the aforementioned reversal of the tip-scanning direction. In contrast, the reversal of the tip magnetization does not affect the resulting toroidization, which corroborates the fact that the MFM-tip field does not contribute to the generation of the net toroidal field. The only function of the tip is to destabilize the spin configuration of individual nanomagnets, and thus to catalyse the poling procedure.

In conclusion, we have created an artificial magneto-toroidal crystal consisting of a two-dimensional array of nanomagnets that are strongly coupled and therefore spontaneously form a ferrotoroidic multi-domain state. This type of long-range order possesses zero net magnetization, yet has a toroidal moment that emerges at the mesoscale. This order parameter is orientated with an effective toroidal field by scanning the array with a magnetized tip. The trajectory of the tip defines the orientation of a locally generated effective toroidal field in the scanned area. The stray field of the tip merely catalyses the poling process by destabilizing the local magnetic configuration, thus promoting its response to the toroidal field. The polability requires the strong coupling between the nanomagnets. Indeed, using the employed poling protocol, the scanning tip cannot convert a single, isolated quadratic unit of our lattice into a toroidal state. This is very different from the case of weakly coupled nanomagnets, where an external perturbation is needed to coerce each magnet separately into a magnetic vortex state of defined handedness[28].

Our array of nanomagnets not only provides a model system designed to access a novel type of magnetization-free, yet polable ferroic state, but also provides a new route to non-reciprocal physical phenomena that are based on the simultaneous violation of spatial and temporal inversion symmetry[30,31]. The sub-micrometre periodicity of our lattice is particularly beneficial as it provides the opportunity for the generation of exotic optical effects[32]. For example, phenomena such as non-reciprocal directional dichroism (that is, the dependence of the absorption of unpolarized light on the direction of propagation, ultimately leading to an 'optical diode'[33]) can be obtained with artificial ferrotoroidic crystals where the optical coefficients are given by the macroscopic domain structure. The twofold space–time symmetry violation and its physical consequences are of general interest, as evidenced by the intense

research on magneto-electric multiferroics, topological materials, polar superconductors and other fascinating states of matter that fall into the same symmetry category[8]. The demonstrated ability to access exotic field configurations and engineer emergent ferroic orders will provide new insights into the formation, control and dynamics of multifunctional materials.

Online content

Any methods, additional references, Nature Research reporting summaries, source data, statements of data availability and associated accession codes are available at https://doi.org/10.1038/s41565-018-0321-x.

Received: 20 August 2018; Accepted: 1 November 2018;
Published online: 10 December 2018

References

1. Sander, D. et al. The 2017 Magnetism Roadmap. *J. Phys. D* **50**, 363001 (2017).
2. Meiklejohn, W. H. & Bean, C. P. New magnetic anisotropy. *Phys. Rev.* **105**, 904 (1957).
3. Nogués, J. & Schuller, I. K. Exchange bias. *J. Magn. Magn. Mater.* **192**, 203–232 (1999).
4. Mostovoy, M. Ferroelectricity in spiral magnets. *Phys. Rev. Lett.* **96**, 067601 (2006).
5. Marti, X. et al. Room-temperature antiferromagnetic memory resistor. *Nat. Mater.* **13**, 367–374 (2014).
6. Jungwirth, T., Marti, X., Wadley, P. & Wunderlich, J. Antiferromagnetic spintronics. *Nat. Nanotech.* **11**, 231–241 (2016).
7. Spaldin, N. A., Fiebig, M. & Mostovoy, M. The toroidal moment in condensed-matter physics and its relation to the magnetoelectric effect. *J. Phys. Condens. Mater.* **20**, 434203 (2008).
8. Fiebig, M., Lottermoser, T., Meier, D. & Trassin, M. The evolution of multiferroics. *Nat. Rev. Mater.* **1**, 16046 (2016).
9. Dubovik, V. M. & Tugushev, V. V. Toroid moments in electrodynamics and solid-state physics. *Phys. Rep.* **187**, 145–202 (1990).
10. Ederer, C. & Spaldin, N. A. Towards a microscopic theory of toroidal moments in bulk periodic crystals. *Phys. Rev. B* **76**, 214404 (2007).
11. Heyderman, L. J. & Stamps, R. L. Artificial ferroic systems: novel functionality from structure, interactions and dynamics. *J. Phys. Condens. Mat.* **25**, 363201 (2013).
12. Nisoli, C., Moessner, R. & Schiffer, P. Colloquium: artificial spin ice: designing and imaging magnetic frustration. *Rev. Mod. Phys.* **85**, 1473–1490 (2013).
13. Van Aken, B. B., Rivera, J.-P., Schmid, H. & Fiebig, M. Observation of ferrotoroidic domains. *Nature* **449**, 702–705 (2007).
14. Zimmermann, A. S., Meier, D. & Fiebig, M. Ferroic nature of magnetic toroidal order. *Nat. Commun.* **5**, 4796 (2014).
15. Tolédano, P. et al. Primary ferrotoroidicity in antiferromagnets. *Phys. Rev. B* **92**, 094431 (2015).
16. Bedanta, S. & Kleemann, W. Supermagnetism. *J. Phys. D* **42**, 013001 (2009).
17. Mengotti, E. et al. Real-space observation of emergent magnetic monopoles and associated Dirac strings in artificial kagome spin ice. *Nat. Phys.* **7**, 68–74 (2011).
18. Anghinolfi, L. et al. Thermodynamic phase transitions in a frustrated magnetic metamaterial. *Nat. Commun.* **6**, 8278 (2015).
19. Kapaklis, V. et al. Thermal fluctuations in artificial spin ice. *Nat. Nanotech.* **9**, 514–519 (2014).
20. Morgan, J. P., Stein, A., Langridge, S. & Marrows, C. H. Thermal ground-state ordering and elementary excitations in artificial magnetic square ice. *Nat. Phys.* **7**, 75–79 (2011).
21. Zhang, S. et al. Crystallites of magnetic charges in artificial spin ice. *Nature* **500**, 553–557 (2013).
22. Farhan, A. et al. Direct observation of thermal relaxation in artificial spin ice. *Phys. Rev. Lett.* **111**, 057204 (2013).
23. Gartside, J. C., Burn, D. M., Cohen, L. F. & Branford, W. R. A novel method for the injection and manipulation of magnetic charge states in nanostructures.*Sci. Rep.* **6**, 32864 (2016).
24. Wang, Y.-L. et al. Rewritable artificial magnetic charge ice. *Science* **352**, 962–966 (2016).
25. Gartside, J. C. et al. Realization of ground state in artificial kagome spin ice via topological defect-driven magnetic writing.*Nat. Nanotech.* **13**, 53–58 (2018).
26. Luttinger, J. M. & Tisza, L. Theory of dipole interaction in crystals. *Phys. Rev.* **70**, 954–964 (1946).
27. Alkadour, B., Mercer, J. I., Whitehead, J. P., Southern, B. W. & van Lierop, J. Dipolar ferromagnetism in three-dimensional superlattices of nanoparticles. *Phys. Rev. B* **95**, 214407 (2017).
28. Jaafar, M. et al. Control of the chirality and polarity of magnetic vortices in triangular nanodots.*Phys. Rev. B* **81**, 054439 (2010).
29. Zheng, Y. & Chen, W. J. Characteristics and controllability of vortices in ferromagnetics, ferroelectrics, and multiferroics. *Rep. Prog. Phys.* **80**, 086501 (2017).
30. Arima, T. Magneto-electric optics in non-centrosymmetric ferromagnets. *J. Phys. Condens. Mater.* **20**, 434211 (2008).
31. Szaller, D., Bordács, S. & Kézsmárki, I.Symmetry conditions for nonreciprocal light propagation in magnetic crystals.*Phys. Rev. B* **87**, 014421 (2013).
32. Tomita, S., Kurosawa, H., Ueda, T. & Sawada, K. Metamaterials with magnetism and chirality. *J. Phys. D* **51**, 083001 (2018).
33. Toyoda, S. et al. One-way transparency of light in multiferroic CuB_2O_4.*Phys. Rev. Lett.* **115**, 267207 (2015).

Acknowledgements

We thank S. Gliga for initial discussions. This work was funded by an ETH Research Grant (grant number ETH-28 14-1 'Resonant optical magnetoelectric effect in magnetic nanostructures' (to J.L. and M.F.)).

Author contributions

All authors contributed to the discussion and interpretation of the experiment. J.L., C.D. and M.F. wrote the manuscript with input from all co-authors. C.D. fabricated the nanomagnetic structures. J.L. performed the LMOKE and MFM experiments and micromagnetic calculations. P.M.D. and J.L. developed the theoretical description. M.F. and L.J.H. supervised the study.

Competing interests

The authors declare no competing interests.

Additional information

Reprints and permissions information is available at www.nature.com/reprints.

Correspondence and requests for materials should be addressed to J.L. or M.F.

Publisher's note: Springer Nature remains neutral with regard to jurisdictional claims in published maps and institutional affiliations.

Methods

Sample fabrication. Two-dimensional artificial magneto-toroidal crystals were patterned on a silicon-(100) substrate using a combination of electron beam lithography and thermal evaporation at room temperature, followed by a lift-off process. A 20-nm-thick permalloy film was deposited through thermal evaporation, and coated with 2 nm of aluminium to prevent oxidation of the sample in air. Four stadium-shaped permalloy ($Ni_{81}Fe_{19}$) nanomagnets with dimensions of $450\times150\times20\,nm^3$ formed the unit cell of a square lattice with a period of 830 nm. To achieve strong dipolar coupling, the edge-to-edge separation between neighbouring magnets was set to 70 nm. The whole toroidal crystal measured $\sim55\times55\,\mu m^2$.

Using permalloy as a ferromagnetic material ensures a negligible magneto-crystalline anisotropy that, together with polycrystalline growth, results in a magnetic state determined by the shape anisotropy. The lateral aspect ratio of 1:3 of the magnets results in Ising-like magnetic moments pointing in one of the two directions parallel to their long edge.

Magnetic manipulation and imaging. Magnetic manipulation and imaging were performed using an NT-MDT NTEGRA magnetic force microscope in semi-contact lift-height mode. The system includes an electromagnet providing an in-plane magnetic field of up to 50 mT, which is used to prepare the [110]-net-magnetized initial state of the nanomagnetic array, as shown in Fig. 2b. For the toroidal poling, an MFM tip with a high magnetic moment (NanoWorld PPP-MFMR) was scanned across the sample. The tips were coated with a cobalt-alloy layer of 40 nm, providing permanent magnetization along the tip axis, which was set using an $Nd_2Fe_{14}B$ permanent magnet. Using these tips, a bidirectional raster scan at $10\,\mu m\,s^{-1}$ tip velocity along the fast axis with a line-to-line spacing of 20 nm was applied for toroidal poling across an area of $12\times12\,\mu m^2$. By scanning the crystal with a tip of low magnetic moment (Nanosensors PPP-LM-MFMR), the magnetic state of our mesoscopic crystal could be probed without altering the direction of magnetization. All imaging was performed with a lift height of 45 nm.

Magneto-optical Kerr effect. Magnetization curves of our array of nanomagnets were measured using LMOKE. A current-stabilized continuous-wave laser diode emitting light at a wavelength of 405 nm and with a power of ~10 mW was used. The light was polarized along $\pm[1\bar{1}0]$ directions and incident at an angle of 45° to the sample normal. The laser was focused to a spot diameter of about 30 µm. The sample was positioned in an electromagnet providing an in-plane magnetic field of up to ±250 mT along the [110] direction. Magnetization curves were obtained by measuring the rotation of the polarization of the reflected light with a Wollaston prism and balanced silicon photodiodes[34].

Calculation of the effective toroidal field. To determine how the toroidal field is generated, we performed micromagnetic calculations based on two-dimensional finite elements. We considered the dipolar interactions of eight nanomagnets: the four central building blocks of a unit cell and the four magnets next to it (see Fig. 3). Contributions from the next-nearest neighbours did not change the result and were therefore neglected. To calculate the net field acting on a tip-destabilized nanomagnet, magnetic stray fields exerted by its seven neighbouring magnets were superimposed. The magnetic field exerted by the MFM tip was not taken into account, as it catalyses the reorientation process but does not determine the new direction of magnetization. The resulting field determined the new magnetization direction of the tip-destabilized magnet. Quantitatively, the magnetic-dipolar field $\mathbf{H}_D(\mathbf{m},\mathbf{r})$ generated by a finite magnetic element with magnetic moment $\mathbf{m}$ located at $\mathbf{r}_0$ was calculated as:

$$\mathbf{H}_D(\mathbf{m},\mathbf{r}) = \frac{1}{4\pi}\left(3\frac{\mathbf{m}\,(\mathbf{r}-\mathbf{r}_0)}{|(\mathbf{r}-\mathbf{r}_0)|^5}(\mathbf{r}-\mathbf{r}_0) - \frac{\mathbf{m}}{|(\mathbf{r}-\mathbf{r}_0)|^3}\right) \quad (1)$$

where $\mathbf{r}$ was measured from the centre of the unit cell. Each nanomagnet was approximated by 2,585 homogeneously magnetized finite elements with dimensions of $5\times5\,nm^2$. As the trajectory of the tip was followed, all four nanomagnets of a unit cell were sequentially destabilized at four different times, shown as τ_1–τ_4 in Fig. 3. To determine the field acting on the respective destabilized magnet, an average (bold red arrows in Fig. 3) of the magnetic field derived from equation (1) (red contours in Fig. 3) was calculated over the area of this magnet. The resulting effective toroidal field $\mathbf{S}_{eff} \equiv \nabla\times\mathbf{H}$ was then obtained according to:

$$\nabla\times\mathbf{H} = \left[\left(\frac{H_{4,y}(x+|r|) - H_{1,y}(x-|r|)}{2|r|}\right) - \left(\frac{H_{2,x}(y+|r|) - H_{3,x}(y-|r|)}{2|r|}\right)\right]\mathbf{e}_z \quad (2)$$

based on the averaged local field component H_i obtained from equation (1). Calculating equation (2) for both scan directions (see Fig. 4), the two opposite orientations of the acting toroidal field $\mathbf{S}_{eff}$ can be verified.

Data availability

The data that support the figures within this paper and other findings of this study are available from the corresponding authors upon reasonable request.

References

34. Hubert, A. & Schäfer, R. *Magnetic Domains: The Analysis of Magnetic Microstructures* (Springer, Berlin & New York, 1998).